In Situ Synchrotron X-ray Diffraction Studies of the Effect of Microstructure on Tensile Behavior and Retained Austenite Stability of Thermo-mechanically Processed Transformation Induced Plasticity Steel

Kun Yan[1], Klaus-Dieter Liss[2,1], Ilana B. Timokhina[3], Elena V. Pereloma[1*]

[1]School of Mechanical, Materials and Mechatronic Engineering, University of Wollongong, NSW 2522, Australia

[2]Australian Nuclear Science and Technology Organisation, Lucas Heights, NSW 2234, Australia

[3]Centre for Material and Fibre Innovation, Deakin University, Geelong, VIC 3217, Australia

* *Corresponding Author*:

Phone: +61 4221 5507

Fax: +61 4221 3662

E-mail: elenap@uow.edu.au

Abstract

Transmission electron microscopy and in situ synchrotron high-energy X-ray diffraction were used to investigate the martensitic transformation and lattice strains under uniaxial tensile loading of Fe-Mn-Si-C-Nb-Mo-Al Transformation Induced Plasticity (TRIP) steel subjected to different thermo-mechanical processing schedules. In contrast with most of the diffraction analysis of TRIP steels reported previously, the diffraction peaks from the martensite phase were separated from the peaks of the ferrite-bainite α-matrix. The volume fraction of retained

γ-austenite, as well as the lattice strain, were determined from the diffraction patterns recorded during tensile deformation. Although significant austenite to martensite transformation starts around the macroscopic yield stress, some austenite grains had already experienced martensitic transformation. Hooke's Law was used to calculate the phase stress of each phase from their lattice strain. The ferrite-bainite α-matrix was observed to yield earlier than austenite and martensite. The discrepancy between integrated phase stresses and experimental macroscopic stress is about 300 MPa. A small increase in carbon concentration in retained austenite at the early stage of deformation was detected, but with further straining a continuous slight decrease in carbon content occurred, indicating that mechanical stability factors, such as grain size, morphology and orientation of the retained austenite, played an important role during the retained austenite to martensite transformation.

Key words: Transformation-induced plasticity steel, Austenite to martensite transformation, Synchrotron X-ray diffraction, High-energy X-rays, Transmission electron microscopy

1. Introduction

Transformation induced plasticity (TRIP) steels were developed and studied intensively in the last 20 years due to their excellent combination of strength and ductility. The typical microstructure of TRIP steel consists of body centered cubic (*bcc*) polygonal ferrite (PF), carbide-free bainite (B) with assumed *bcc* lattice due to low carbon content, face centered cubic (*fcc*) retained austenite (RA) and α´-martensite (M) phase, which could possess either *bcc* or body centered tetragonal (*bct*) lattice structure depending on carbon content. As a result of the multi-phase microstructure as well as the transformation from metastable retained austenite to martensite phase during straining, the outstanding mechanical properties of ultimate tensile strength (~1000 MPa) and elongation (~40 %) make TRIP steel a promising candidate for the automotive industry. It is believed that an increase in the volume fraction of retained austenite increases the strain-hardening coefficient, which leads to an increase in elongation [1]. In addition, the supersaturation of carbon in the RA determines the chemical stability, whereas the size and morphology of RA grains controls the mechanical stability [2-5]. Therefore, previous research work concentrated on how to adjust the parameters during thermo-mechanical processing [1, 3, 5] or thermal stimulation [6] to produce a TRIP steel with the microstructure that favors gradual transformation from retained austenite to martensite phase.

As advanced microstructural characterization tools, synchrotron high-energy X-ray [7, 8] and neutron diffraction [6, 9-11] have been applied to investigate the evolution of TRIP steels microstructures during in situ straining and in real time. Three major questions are targeted for in situ investigations of TRIP steels using synchrotron X-ray and neutron diffraction: (i) the change of phase volume fraction with plastic deformation[12-14]; (ii) the strain and stress behaviour of different phases, as well as the interaction between these phases

during straining[10, 11, 13, 15]; (iii) the change of lattice parameter for the retained austenite, which includes strain caused by both mechanical straining and changes in chemical concentration [6, 14]. These investigations provide direct evidence of individual phases accommodating the external stress at different deformation stages, which is also known as load partitioning among phases, as well as the relation between grain orientation and the RA to martensite phase transformation [9].

However, for most cases, the lattice strain of the martensite phase is inaccessible due to overlapping diffraction peaks of the *bcc/bct* martensite and the *bcc* α-matrix containing polygonal ferrite and bainite. Although there are a number of studies [16-21] that have been attempted the separation martensite from α-matrix, most of reported studies chose to treat martensite phase as part of the α-matrix. In the latter case, the law of mixtures [22] is employed to acquire the martensite phase stress by deducting the phase stress of austenite and α-matrix from macroscopic stress [12]. Moreover, the high penetration depth of synchrotron and neutron diffraction allows delineating the peak shift associated with carbon concentration [6].

In the current study, two TRIP steel specimens with different microstructures obtained from thermo-mechanical processing, were investigated by synchrotron X-ray diffraction during tensile deformation. The volume fraction of the retained austenite γ-phase is recorded with the strain level of tensile deformation. In contrast with most of the previous studies, the martensite phase (α′) was separated from the ferrite-bainite matrix (α) in the current study, which explained the deviation between the integrated phase stresses calculated from strain behavior and the experimentally measured macroscopic stress. In addition, the authors have proposed an approach in deducting the lattice strain caused by macroscopic deformation and have further calculated the change in carbon concentration within the retained austenite phase during tensile deformation. Consequently, the relationship between microstructure and

mechanical properties of the two specimens were analyzed and interpreted.

2. Experimental procedures

2.1 Materials processing and microscopy observations

TRIP steel with composition listed in Table 1 was used in this study. Plate-shaped ingots were subjected to laboratory simulations of thermo-mechanical processing (TMP) using a laboratory rolling mill at Deakin University. After reheating to 1250 °C and holding for 1800 s in a 15 kW muffle furnace, the plates were rolled immediately to 25 % reduction at 1100 °C, held for 120 s to condition the austenite microstructure, then cooled at 2 K/s to 875 °C, where the second deformation of 47 % reduction was applied. In order to form various volume fractions of polygonal ferrite (PF), slow cooling at 1K/s after the second deformation through the ferrite formation region was interrupted at two temperatures (770 °C and 790 °C) by water mist cooling at 20 K/s to 500 °C. Following this, the plates were placed into a fluidized bed furnace and covered with aluminum oxide sand for a hold at 470 °C for 1200 s. This step in the processing simulated coiling and allows for the bainite transformation to take place. After this step, the plates were water quenched. Hereafter, the obtained samples are referred to as TMP-770 and TMP-790, based on the temperatures used in their schedules for the interrupted PF formation.

After TMP the samples were characterized using optical microscopy and transmission electron microscopy (TEM). The samples were sectioned along the deformation direction (ND-RD plane) for optical microscopy and perpendicular to the rolling direction (ND-TD plane) for TEM studies. To reveal all the phases present in the microstructure a heat tinting technique was applied [1], as it allowed the separation of martensite and austenite phases. With this technique polygonal ferrite and bainitic ferrite appear in light/beige color, whereas martensite was blue and retained austenite was maroon/purple. Thin foils for TEM

investigation were prepared using solution of 5 % perchloric acid in methanol at - 20 °C and an operating voltage of 30 V in a twin-jet electro-polisher. TEM investigation was carried out on a PHILIPS® CM20 microscope operating at 200 kV.

2.2 Diffraction measurements

Tensile samples with $\sim 4 \times 2\ mm^2$ cross-section and ~10 mm gauge length were machined for in situ observations during tensile loading using the high-energy X-ray diffraction beamline, 1-ID of the Advanced Photon Source (Argonne National Laboratory, IL, USA). High energy X-rays of 92.3 keV were used in a typical setup for thermo-mechanical processing in a synchrotron beam and was identical to those described in [23]. Corresponding wavelength and wave-number were 0.134 Å and 46.7 $Å^{-1}$, respectively. The specimens were put into a servo-hydraulic load frame with the load axis perpendicular to the incoming X-ray beam of $100 \times 100\ \mu m^2$ size. Specimens were aligned with the rolling normal direction (ND) parallel to the beam. Two-dimensional diffraction patterns were recorded by a quadratic GE flat panel detector of 410 mm slide length and 200 μm quadratic pixel size in 1114 mm distance, covering full Debye-Scherrer rings up to 8.5 $Å^{-1}$ along the axes and 12 $Å^{-1}$ along the diagonal. The center of the detector was shaded out to ~3.1 $Å^{-1}$ by a thin Pb foil in order to attenuate the strong α-110 reflection. Due to small Bragg angles between 2° and 5° orientations close to the longitudinal (LD) and transverse (TD) directions, these directions were probed and recorded continuously every 11 s upon application of load. The entire load frame has been continuously translated vertically to adjust the beam impinging a fixed sample position, while the strain was increased. Further details of the experimental setup and measurement can be found in Ref [8].

2.3 Diffraction data analysis

The full, two-dimensional Debye-Scherrer diffraction rings showed a smoothly varying intensity distribution, proving signal from a high number and highly distorted grains within the illuminated volume of $0.1 \times 0.1 \times 2$ mm^3, as necessary for both quantitative phase and texture analysis [8]. This powder averaging approach is consistent with the 1-10 μm grain size distribution in the studied material, which contains defects resulting from TMP and phase transformations. Displacement of the sample with respect to the beam did not lead to significant fluctuations in the data. The in situ diffraction rings were azimuthally integrated into N sectors to obtain azimuthally orientation-dependent powder diffraction patterns and to extract the following three types of information:

(1) Phase identification and volume fraction. In this category, diffraction intensity was integrated along the azimuthal angle into N = 1 sector and the diffraction patterns were obtained as shown in Fig. 1a. Crystallographic reflections belonging to the *fcc* and *bcc* phases were identified and indicated in Fig. 1a. By stacking all the integrated diffraction patterns with time, the change in diffraction intensity with tensile deformation can be observed in Fig. 1b. In particular, the components of the *bcc* reflections in the diffraction patterns have been fitted simultaneously by two overlapping Voigt functions and thus deconvoluted into two peaks that are dedicated to the ferrite and bainite matrix (α-matrix) and the α′-martensite phase, as displayed in Fig. 1c. The detailed fitting procedure includes the following steps: (i) First, the authors tried to fit the diffraction pattern with martensite phase of *bct* structure, however, a significant mismatch was observed between the experimentally measured and the calculated diffraction patterns. Therefore the crystallographic structure of martensite was assumed to be *bcc* but with lattice parameters slightly different from the ones of ferrite due to a much higher carbon content [3]; (ii) Ignoring the extra peaks and asymmetry of diffraction peaks caused by martensite, the whole

pattern was fitted by only *bcc* α-matrix and *fcc* austenite. This procedure delivers the lattice strain data for both *bcc* matrix and *fcc* austenite. (iii) Fit the asymmetric, broad *bcc* peaks by de-convoluting into two peaks with two Pseudo-Voigt functions, from which the lattice parameters of the α-matrix and the martensite were obtained. (iv) In the elastic region, the difference in slopes of various *hkl* reflections, deliver lattice strain-stress responses in the elastic range below the elastic limit. This is due to the cubic elastic anisotropy and consequent elastic load sharing among variously oriented families of polycrystal grains. For a cubic structure, these slopes are proportional to the cubic elastic anisotropy factor

$$A_{hkl} = \frac{(h^2k^2 + k^2l^2 + l^2h^2)}{(h^2 + k^2 + l^2)^2} \quad (1)$$

where *h, k, l* are the Miller indexes[12, 24]. For instance, in the *bcc* matrix the trend of A_{hkl} factor is $A_{200}<A_{310}<A_{220}$, comparatively, for *fcc* austenite this sequence should be $A_{200}<A_{311}<A_{220}$. From the results, the lattice strain of the α-matrix, austenite and martensite can be calculated and the elastic anisotropy of these phases are compared to the theoretical elastic anisotropy factor A_{hkl}, mentioned above;

(2) In order to investigate the lattice strain of various planes with their normal direction parallel (∥) and perpendicular (⊥) to the loading direction, sectors of 15°, centered around azimuthal angle Ψ = 0 and 180° were selected from each 2D diffraction image to represent LD, and in counterpart along Ψ = 90° and 270° for TD. Selected reflections, γ-200, γ-220 and γ-311 for the *fcc* austenite, as well as α-200, α-211, α-220 and α-310 for the *bcc* α-matrix were fitted by Voigt functions. By single peak fitting, the lattice plane strain for the *hkl* reflection was calculated by

$$\varepsilon_{hkl} = \frac{d - d_0}{d_0} \quad (2)$$

where d and d_0 are the lattice plane distance at the moment of observation and of as-received

material, respectively.

In addition, the weighted average phase strain ε_{ph} was calculated by

$$\varepsilon_{ph} = \frac{a - a_0}{a_0} \tag{3}$$

where a represents the crystallographic lattice parameter obtained from weighted averaging of the measured lattice parameter as described by

$$a = \sum_{hkl} f_{hkl} \cdot a_{hkl} \tag{4}$$

Where f_{hkl} represents the intensity volume fraction of the *hkl* reflection and a_{hkl} is the lattice parameter calculated from the peak position of reflection *hkl*. The lattice parameters a_0 for each phase before tensile deformation in Eq. (3) were obtained from the diffraction patterns prior to the onset of macroscopic loading.

(3) Along the azimuthal direction, the Debye-Scherrer rings were sectioned starting from the loading direction with a step of 2°. In each section, the diffraction intensity was summed along the azimuthal angle and resulted in N=180 diffraction patterns. The change of peak position as a function of azimuthal angle was obtained by single peak fitting. These results were used to find the orientation at which the crystallographic lattice was not affected by macroscopic loading, thereafter to ascertain the impact of carbon concentration change on the austenite phase lattice parameter during tensile deformation.

3. Results

3.1 Microstructure and macroscopic strain-stress behavior

The optical micrographs after TMP schedules of heat-tinted samples are shown in Fig. 2. The microstructure of both samples TMP-790 and TMP-770 consisted of polygonal

ferrite, carbide-free bainite, retained austenite and martensite. As expected, the volume fraction of the PF was different in these two samples: ~19 and 30% in samples TMP-790 and TMP-770, respectively. In addition, the PF grains were finer in sample TMP-790 compared to sample TMP-770, as they had less time to grow in the former due to the early application of accelerated cooling. The RA grains were located between the PF grains, at the interfaces between the PF and bainite and within the bainite regions.

A more detailed insight into the morphologies of the phases is given by TEM (Fig. 3). The equiaxed PF grains have the lowest dislocation density, whereas neighbor plate or lath-like crystals of bainitic ferrite have higher dislocation density. Laths of BF were separated by the layers of martensite or retained austenite (Fig. 3a,b,c). The thickness of these layers varied from 0.07μm to 0.3μm. The regions with granular bainite (GB) morphology contained BF plates with blocky RA, M or M/RA constituent (Fig. 3e,f). In addition, in the TMP-790 sample the bainitic ferrite laths and plates were oriented in various directions, whereas in TMP-770 many regions with parallel bainitic laths were observed. Martensite crystals display two internal structures: those containing high-density dislocation substructure (Figs. 3a-c) and those containing additional twins (Fig. 3g). These two morphologies were correlated with their formation from parent austenite with lower or higher carbon content, respectively.

The macroscopic stress-strain curves for the samples TMP-770 and TMP-790 are shown in Fig. 4a. Since there are no obvious yielding points on the strain-stress curves of sample TMP-770 and TMP-790, the macroscopic yielding point is taken at 0.002 of true strain. Therefore, the 0.2% proof stress of 680MPa, ultimate tensile strength of 1051 MPa and total elongation of 21% were obtained for sample TMP-770, while TMP-790 yielded at 695MPa and achieved elongation up to 25% with tensile strength of 1119 MPa (Table 2).

Fig. 4b demonstrates the evolution of the incremental work-hardening exponent n_{incr} as a function of true strain from a true strain of 0.01, until the end of uniform elongation.

Initially, the n_{incr} of specimen TMP-790 and TMP-770 both increased with tensile strain. After reaching the maximum n_{incr} at true strain equal to 0.035 (as the green dashed line indicated in Fig. 4b), n_{incr} for both samples decreased continuously with increasing tensile deformation, where the n_{incr} of TMP-790 dropped to a greater level and at a faster rate than TMP-770. Combining the evolution of n_{incr} with the stress-strain behavior of TMP-790 and TMP-770, it appeared that the higher n_{incr} leads to higher yield stress, ultimate stress and elongation in sample TMP-790.

3.2 Evolution of the austenite phase volume fraction

The volume fraction of austenite was calculated from whole-pattern fitting and displayed in Fig. 4c. The transformation of the RA in TMP-790 starts at higher stress (~650 MPa) and strain than in TMP-770 (~610 MPa). Before tensile deformation, there was 11.5 vol. % of austenite in TMP-770 while this number is 9 vol. % in TMP-790. However, the RA in TMP-790 was less stable and practically all transformed into martensite during tensile deformation with only 0.32 vol. % remaining untransformed. In comparison, a slightly higher volume fraction of ~1.46 vol. % was present in the microstructure of TMP-770 after fracture.

To estimate how much of the retained austenite changed with true strain, the normalized austenite phase was calculated by $\frac{V\gamma - V\gamma_{\varepsilon_u}}{V\gamma_0 - V\gamma_{\varepsilon_u}}$, where $V\gamma$ is the volume fraction of retained austenite at a given true strain level, $V\gamma\varepsilon_u$ is the volume fraction of retained austenite at ultimate tensile strength (UTS), $V\gamma_0$ is the initial volume fraction of retained austenite before deformation [25]. This normalized ratio is presented in Fig. 4b, where it is clear that TMP-770 and TMP-790 have very similar behavior from the true strain of 0.002 to 0.067 (where the blue dashed line is drawn). Thereafter, the transformation of the remaining

austenite into martensite in TMP-770 becomes slightly faster than that in sample TMP-790. From a true strain equal to 0.125 and onwards (where the red dashed line is in Fig. 4b), the transformation of retained austenite in sample TMP-770 is seen to occur much faster than in sample TMP-790.

3.3 Load partitioning between RA, α-matrix and martensite phase

3.3.1 Lattice strain of different reflections in α-matrix and austenite phase change with true strain

Before the phase stresses of austenite, α-matrix and α′-martensite were calculated, the lattice strains were computed by Eq. (2) and the weighted average phase strain was determined by Eq. (3). Fig. 5a displays the change of lattice strains of individual grain families {200}, {211}, {220} and {310} in α-matrix with true strain in sample TMP-790. The grain family with {200} lattice planes perpendicular to LD displays the highest lattice strain, while the family with {220} lattice planes perpendicular to LD demonstrates the lowest lattice strain. This can be explained by the elastic anisotropy factor of the cubic crystallographic structure [10]. The orientations with a high directional strength-to-stiffness ratio will yield later than orientations with a low directional strength-to-stiffness ratio. As could be seen from Fig.5a, {220} grains yield first, whereas {200} grains yield last. Similarly, the lattice strain of grain families {311}, {200} and {220} in austenite phase also behaved differently with increasing macroscopic strain (Fig. 5b). The lattice strains in both α-matrix and γ-austenite exhibit different stages of deformation, which are evident by the change in the slope. The first linear region corresponds to the elastic loading, followed by the elastic-plastic transition region. Finally, the last nearly linear region is contributed to plastic deformation, which follows complete yielding [26].

As shown in Fig. 5b, the {200} grain family exposes the highest lattice strain being the most elastically compliant [26], which is also the last to yield. The scatter in lattice strain data increases with strain, especially for the {220} grain family, because the γ volume fraction ceases and the X-ray signal statistics becomes noisier. In particular, texture plays a role, being associated with a progressive rotation of {220} grains to the <111> fiber, such that some reflections become very weak in LD- or TD-direction [27]. The phase strains, which are the weighted averages over all the major reflections shown in Figs. 5a and 5b, were calculated and shown as red dashed lines, demonstrating, how each phase evolves with external deformation.

It is worth to point out that the lattice strain of the {200} and {310} grain families of the α-matrix along TD direction become less compressive or even slightly tensile after passing the yielding point (in Fig 5a). This phenomenon has been reported numerous times [6, 12, 20, 21, 28-30]. Even when the texture effect was excluded by rotating specimen during in-situ X-ray diffraction, "tensile lattice strain" of ferrite phase along transverse direction was still observed [6]. The observed tensile lattice strain along the transverse direction is caused by the tensile specimen's initial condition and the choice of the reference lattice parameter d_0. In the present case, the authors used the initial lattice spacings of the *bcc* phase along LD and TD as d_0 for lattice strain calculation. It should be noted that the tensile specimen was processed by thermomechanical processing; certain level of inter-granular and inter-phase residual stress was found to result from its previous processing procedure. After processing stress was relieved, some grain families conserve tensile, others compressive biases, which is known to be the driving force for the Bauschinger effect.

3.3.2 Evolution of phase lattice strain for three phases as a function of engineering stress

In Fig. 6a, b, the changes of phase strain along LD and TD are plotted against engineering stress for sample TMP-770 and TMP-790. However, it is worth noting that there

was some martensite phase in both TMP-770 and TMP-790 before tensile deformation (Fig. 3), which we term the original martensite phase. Among these three phases, the α-matrix has always the lowest overall lattice strain value, at all times and for both specimens. The development of lattice strain for austenite and martensite are fairly similar before the proof stress, however the lattice strain of martensite continues to increase with external loading while the lattice strain of austenite maintains constant and slightly reduces with increasing load. The lattice strain of martensite in sample TMP-770 changes on a smaller scale with external load at the elastic and elasto-plastic region than in sample TMP-790.

3.3.3 Load partitioning between austenite phase and α-matrix

In order to investigate the lattice strain behavior of the austenite phase and the α-matrix, together with the austenite to martensite phase transformation as a function of external load, the phase lattice strains of α-matrix and austenite were plotted against engineering stress in Fig. 7. The lattice strain vs engineering stress curves were separated into three sections: an elastic region from 0 MPa to σ_E, an elasto-plastic region from σ_E to proof stress $\sigma_{0.2}$ and a plastic region from $\sigma_{0.2}$ to ultimate tensile stress. In addition, the starting macroscopic stress of the austenite to martensite phase transformation was annotated in Figs. 7b,d.

To demonstrate the deviation of phase lattice strain from linear change with engineering stress, asymptotes to zero were added to Fig.7 as straight dashed lines. In Fig. 7a,c, the α-matrix lattice strain deviates from linearity the earliest at 275 MPa for TMP-770 and 280 MPa for TMP-790. Comparatively, for austenite it deviates at 320 MPa for TMP-770 and 335 MPa for TMP-790. Furthermore is found in Figs. 7b, d that the austenite to martensite phase transformation starts earlier than reaching macroscopic proof stress. It is worth to recall that the starting point of austenite to martensite phase transformation has been

detected by the reduction of the austenite volume fraction, obtained from the diffraction patterns that were integrated over all directions on the Debye-Scherrer ring. Therefore, although the resolved plane stress along LD is expected to be the largest among all the Debye-Scherrer azimuthal angles, the austenite to martensite transformation may occur earlier in grains with other orientations, depending on the angle between the external load and the shear orientation on the shear plane. Nevertheless, the increase of austenite lattice strain slows down after reaching the phase transformation stress of 610 MPa in sample TMP-770. After start of the austenite to martensite phase transformation, austenite lattice strain along LD still increases with macroscopic stress until the lattice strain reaches the value of 5.4×10^{-3} for TMP-770 and 5.6×10^{-3} for TMP-790. Afterwards, the lattice strain of austenite enters a plateau zone until the ultimate tensile strength is achieved. For both samples, their austenite phase reaches the saturation of lattice strain increases with macroscopic stress at about 800-810 MPa. It indicates the end of load distribution between the austenite and α-matrix and the start at this point of deformation-assisted austenite to martensite transformation along the LD. The macroscopic strain corresponding to the stress of 800-810 MPa is 0.02.

In correlation to the curve of austenite volume change vs true strain, presented in Fig. 4b, it is found that at strain of 0.02, already 39% of the available austenite in TMP-770 has transformed to martensite. A similar number of 32% was found for sample TMP-790. This means that about one third of the originally present austenite has transformed to martensite before the load redistribution between austenite and α-matrix finishes. This is due to the anisotropy among the different grain families of austenite in respect of their orientations against the external load. The same phenomenon has been reported by Muranski *et al.* [10], where 20-30% of the austenite phase has transformed to martensite before the end of the load redistribution period.

3.3.4 Phase stress, integrated phase stress and microscopic engineering stress

Now, from the phase strain presented in Fig. 6, the phase stress can be ascertained via Hooke's law [13]:

$$\sigma_{11}^{ph} = \frac{E^{ph}}{(1+\nu^{ph})(1-2\nu^{ph})}[(1-\nu^{ph})\varepsilon_{11}^{ph} + \nu^{ph}(\varepsilon_{22}^{ph} + \varepsilon_{33}^{ph})] \quad (5)$$

where σ_{11}represents the stress along loading direction while ε_{22} and $\varepsilon_{33}$are the strains along the transverse direction and normal direction in the measurements. Poisson's ratio (ν) of the α-matrix and RA was estimated as 0.288 and 0.367, respectively. For martensite, Poisson's ratio $\nu^{\alpha'} = 0.2921$ was taken from Ref [31]. Literature values of the Young's modulus (E) for α-matrix, austenite and martensite are 220, 210 and 203.5 GPa [12].

After calculating the phase stress by Hooke's law, the load shared by each individual phase σ_{share}^{ph} was obtained by Eq. (6), where V_f is the volume fraction of each phase changing during tensile deformation.

$$\sigma_{share}^{ph} = V_f \sigma_{11}^{ph} \quad (6)$$

The integrated phase stress was calculated by adding the stress shared by α-matrix and austenite phase together via the low of mixture [13]. The stress shared by the α-matrix, the integrated phase stress and the macroscopic stress for sample TMP-770 and TMP-790 are presented in Figs. 8a, b. To assist the explanation, the proof stresses $\sigma_{0.2}$ were indicated as dashed lines in Fig. 8. First of all, the shared phase stress and the integrated phase stress from the start up to the engineering strain of 0.2% was considered, which is the transition point from elasto-plastic to plastic deformation region. After the material enters the plastic deformation region, the lattice strain changes with external stress will no longer be linear; therefore the Hooke's law cannot be applied to the phase stress calculation. Secondly, from zero stress to the end of the elastic region, which is 275 MPa and 280 MPa for sample TMP-

770 and TMP-790, the development of macroscopic stress shows good agreement with the integrated phase stress and the α-matrix phase stress. However, both the α-matrix stress and the integrated phase stress deviate from the macroscopic stress within the elasto-plastic region. This deviation point occurs much earlier in TMP-770 than in TMP-790. As described before, the austenite to martensite phase transformation started at a macroscopic stress level of 610 MPa for TMP-770 and 650 MPa for TMP-790. For sample TMP-770, the integrated phase stress deviates much earlier before its austenite to martensite phase transformation point, which indicates that load taken by α-matrix has been transformed to austenite phase. Comparatively, the load redistribution between α-matrix to austenite is much quicker in sample TMP-790.

4. Discussion

4.1 Mechanical responses and microstructure

The data directly correlate enhanced plasticity with the progression of retained austenite to martensite transition. The total elongation is slightly lower for the TMP-770 sample (~21 %) as compared to TMP-790 (~25 %), revealed by the stress-strain curves. This may be attributed to the gradual transformation of the RA to martensite during straining in the latter and thus contributing to the TRIP effect, whereas more of the RA remains untransformed in the TMP-770 sample.

The earlier start of the RA transformation in the sample TMP-770 might be associated with the non-uniform distribution of carbon in the RA, due to its location and different local stress transfer from the work-hardened ferrite. In the microstructure of this sample, a significant number of the RA crystals were located in the vicinity of the PF grains and benefited only from the carbon rejection from the PF. Whereas, the RA crystals located in the

BF regions benefited from the additional carbon rejection from the BF. Similar dependence on their location in the microstructure of the RA grains transformation to martensite was reported previously [32]. The delayed start of the RA transformation in the sample TMP-790 could be associated with the delay in work hardening of bainitic ferrite, in comparison with the PF, and subsequently in the load transfer to the RA crystals, which have BF as a neighboring phase. In addition, the microstructure in general and the RA crystals in particular, are more refined in sample TMP-790 as compared to TMP-770. Furthermore, as was reported previously [1] that multi-directional alignment of BF laths, which is a characteristic of TMP-790 sample, delays load transfer to the RA. On the other hand, a parallel arrangement of rigid laths (as in TMP-770) may accelerate this, hence resulting in earlier transformation of RA to martensite.

The strength of sample TMP-790 (1119 MPa) is slightly higher than that of sample TMP-770 (1051 MPa), due to the lower volume fraction of relatively soft PF phase. Similar to the results obtained by others on the mechanical behavior of TRIP steel [33, 34], the ferrite grains yield first, followed by the bainitic ferrite and austenite which start to yield later. It is also worth noting, that in both samples the RA starts transforming to martensite below the proof stress value of ~695 MPa for sample TMP-790 and ~680 MPa for sample TMP-770, respectively. This could be an indication of stress-induced, not strain-induced transformation of the RA to martensite. However, due to the complex multiphase microstructure of the steels studied, the material and the RA crystals in particular started to yield locally at different microscopic stress values. Thus, in the elastic-plastic transition region, the onset of the martensite formation at stresses below the average proof stress of the material were detected, but these stress values may correspond to the yield values of a particular retained austenite crystal. With respect to the two material conditions studied in this work, sample TMP-790 with ~19% PF and ~9% RA exhibits better combination of strength and ductility due to

continuous transformation of the RA to martensite.

4.2 Chemical stability of retained austenite

After TMP treatment, the lattice parameter of RA phase was measured to be a = 3.620 Å for TMP-770 and a = 3.613 Å for TMP-790. However, this lattice parameter varies from 3.6014 to 3.639 Å for TMP-770 and from 3.5935 to 3.6310 Å for TMP-790. Apart from local and orientation-dependent strain variation, differences in chemical concentration were also believed to cause the variance of lattice parameter for RA phase. During tensile loading, the RA gradually transformed to martensite phase. Conventionally, it is believed that the RA grains that contain lower carbon concentration are less stable with respect to the martensitic transformation [13, 35] and transform selectively, so that with progressing transformation, the average carbon concentration of the remaining RA grains increases with decreasing volume fraction of RA. The lattice parameter of RA is linearized, proportional to the concentration of carbon [36, 37] and attention is paid in separating the diffraction peak shift caused by mechanical strain and the chemical composition. The in situ synchrotron X-ray or neutron diffraction measurements, which are able to provide materials crystallographic information along relevant stress directions, appears to shine a light in separating the diffraction peak shift caused by mechanical strain and the change of carbon concentration. Blonde *et al.* [6] combines the lattice strain contributed by deformation and chemical concentration to Hooke's law and derived the lattice strain caused by carbon concentration ε_C from the following formula:

$$\varepsilon_C = \frac{\varepsilon_{TD} + \nu\varepsilon_{LD}}{(1+\nu)} \tag{7}$$

where ε_{LD} and ε_{TD} are the experimental measured lattice strain along loading direction and transverse direction and ν is Poisson's ratio for austenite phase.

The Poisson ratios ν^{α} for α-matrix and ν^{γ} for RA in Eq.(5) were determined from ε vs $\sin^2(\Psi)$ plots, demonstrated in Figure 9. Such plots describe the strain ellipsoid and manifest a straight line in a fully isotropic material [38], when Ψ is measured from one of the main axes of the ellipsoid. With increasing external load, lattice planes with their normal direction parallel to LD are extended; at the same time, the lattice planes having their normal direction perpendicular to LD are compressed. Consequently, the Debye-Scherrer rings are no longer circles but become eclipses with different eccentricity. Furthermore, in anisotropic media, i.e. crystalline material, lattice response is orientation dependent and the shape may deviate from perfect ellipses [8]. Because of strains in LD and TD are always of opposite sign, there exists an orientation, where lattice strain is zero, given in a perfect ellipsoid by Eq. (7), i.e. among those Debye-Scherrer rings from one reflection, there is one fixed point of zero elastic strain, which does not move during the elastic deformation, indicating the best possible point to calculate the carbon concentration during plastic deformation. It is indicated by the dashed lines shown in Figs. 9a,b, where $\sin^2(\Psi) = 0.718$. After yielding, crystallographic anisotropy plays a larger role and the ellipses change shape to more complicated curves, where the plot of lattice strain against $\sin^2(\Psi)$ is no longer linear [8]. The non-linearity strongly depends on the considered lattice plane family and is minimal for {211} for α-matrix and {311} for austenite, which we chose for evaluation, as displayed in Figs. 9c,d. For the two specimens studied, Poisson's ratio of the α-matrix and RA were estimated to be 0.288 and 0.367, respectively, through $\nu = -\varepsilon_{TD} / \varepsilon_{LD}$.

In the current study, it was found that the lattice parameter of RA grains with their {311} reciprocal lattice vector oriented at Ψ=58°, 122°, 238° and 302° were not affected by macroscopic stress (Fig. 7). Therefore, the lattice parameter change of these RA grain orientations should only be attributed to chemical concentration. Taking the sections of

$\Psi = 58°$, 122°, 238° and 302° only, the lattice parameter of austenite phase in sample TMP-770 and TMP-790 were fitted, thereafter the lattice strain was calculated and plotted against macroscopic true strain in Fig. 10. The carbon concentration change was converted from lattice strain and is presented on the right axis of Fig. 10. For comparison, ε_c was calculated from Eq. (7) and is also presented in Fig. 10. The fluctuations at high strain values are due to increasing error, stemming mainly from ceasing austenite reflections and X-ray detection limits.

In contrast with the results reported in [6, 37], where continuous, increase in carbon content was reported for the remaining austenite grains with progress of the austenite to martensite phase transformation, we observe only a small increment of positive lattice strain, which may be due to selective transformation of lesser carbon-contained grains, from the start of loading until 0.002 of engineering strain for sample TMP-770 and until 0.005 for sample TMP-790 (Fig. 10). From these points onwards, ε_c decreases continuously in both specimens with macroscopic engineering strain, until the end of the tensile deformation. Despite the initial increases, the change in lattice strain caused by the change of carbon concentration was approximately -1×10^{-3} in sample TMP-770 and -0.5×10^{-3} in TMP-790. A good agreement was achieved between the method used in the current study and the approach reported in Ref [6], which, in principle, are similar. The difference in method is that Blonde *et al.* [6] treat the strain ellipsoid in a fully linear and isotropic way, while our approach allows to fit both the main axes, i.e. the orientation of the strain ellipsoid and to reveal non-linearities and anisotropies. Particularly, with the large amount of initial residual phase stresses and at large strain values, this plays a more important role.

This experimental result and controversy with literature warrants the revisiting of the topic on carbon-stabilization of austenite phase during the austenite to martensite phase transformation. In the past decades, the relationship between carbon concentration and

stability of the austenite phase during martensitic transformation has been widely investigated. Two mechanisms were introduced to explain how carbon stabilizes the austenite phase, these are described as follows: (i) low carbon concentration austenite has low martensite formation temperature [39]; (ii) the stabilization can be caused by an increase in the resistance of austenite to the growth of martensite, due to the formation of carbon clusters during slow quenching or during isothermal holding [40]. In addition, C also affects the stacking fault energy, which on reaching a certain value will initiate the twinning of austenite as a preferential response to deformation instead of transformation to martensite. During deformation-induced austenite to martensite transformation, the lowering of the martensitic transformation start temperature M_s by addition of specific alloying elements, such as carbon, leads to an increase in mechanical driving force needed for the deformation-induced transformation at the temperatures equal to or greater than room temperature. Thus, during processing of TRIP steels, it is necessary to avoid formation of phases (pearlite or carbide-containing bainites), which could consume carbon, in order to ensure a high C content in the RA and its chemical stability. If following the accepted viewpoint that the RA grains with lower C concentration transform to martensite earlier, then remaining RA would show higher and higher C concentration with ongoing deformation. The lattice parameter change of RA obtained by diffraction methods is widely used to detect the C concentration of RA. For example, Itami *et al.* [41] noted that the portion of the RA that transformed first had a smaller lattice parameter, which corresponds to a lower C content compared to the remaining RA at higher strains. Furthermore, they found that the volume fraction of the RA with lower C content (~0.9 %) reduced at a faster rate at relatively low strains, compared to the more gradual transformation of the RA with higher C content (~1.1 %) to martensite. A trend in the increase in C content of RA with the progress of deformation was also reported in some other works [6, 42].

Although carbon is the strongest austenite stabilizer, other alloying elements present in TRIP steel could additionally affect the chemical stability of RA. As reported recently [43], despite being also austenite stabilizer, inhomogeneous distribution of Mn within RA grain could trigger earlier martensite formation due to the substitution of Fe by Mn atoms and this will cause an increase in lattice expansion leading to local strain.

Furthermore, apart from the lattice strain introduced by external straining, there might be other factors that diminish the lattice parameter expansion caused by increasing carbon concentration. Previous studies [44, 45] reported that the main change in the average C concentration of the RA takes place early on in the deformation process. At later stages, the C content either remains constant or declines while the volume fraction of the RA continuous to decrease.

In addition to the effect of C content, other factors including RA size, morphology and distribution, orientation, the nature of neighboring phases, defect structure, rotation and stress state, affect the mechanical stabilization of the RA and also control its stability during straining. With correlation to the current study, in which the C concentration in the RA was found to increase at the start of deformation but decline gradually afterwards, this indicated that the chemical stabilization played a lesser role than mechanical stabilization during the latter stages of deformation.

5. Conclusions

The phase strain evolution and the stability of retained austenite of two thermo-mechanically processed Fe-Nb-Mo-Al TRIP steels during tensile deformation were investigated by in situ synchrotron high-energy X-ray diffraction measurements and TEM. The conclusions are summarized as follows:

- After thermo-mechanical processing, both specimens TMP-770 and TMP-790 contained polygonal ferrite, bainite, retained austenite and martensite. The specimen TMP-790, which was cooled through the ferrite region from a higher temperature (790˚C), contained a lower volume fraction of polygonal ferrite (19 vs 30%) and retained austenite (9 vs 11.5%) phases than TMP-770 sample.
- During tensile deformation, despite the fact that the retained austenite to martensite transformation rate was faster in specimen TMP-770 than in TMP-790, more retained austenite transformed to martensite in the latter, resulting in a higher incremental work-hardening exponent and a larger elongation. Even though the martensite phase stress was accounted for, the integrated phase stress estimated via the law of mixtures is 300-400 MPa lower than the macroscopic stress. This difference was attributed to the contribution of work-hardening of the individual micro-constituents and the extra hardening of α-matrix and austenite caused by the accommodation of dislocations surrounding the strain-induced martensite.
- Among α-matrix, austenite and martensite phases, the load bearing capacity was the lowest in the α-matrix (ferrite and bainitic ferrite), followed by austenite and then by martensite. The load transfer among phases relates to both the phase volume fraction and the microstructure of the phases. The retained austenite in specimen TMP-790 transformed to martensite at a later stage compared with the TMP-770 due to the combination of (i) the higher volume fraction of bainitic ferrite which was related to a delayed work-hardening of the *bcc* α-matrix; and (ii) a finer microstructure.
- In terms of the retained austenite phase stability, the current study suggests that carbon concentration in retained austenite plays important role only during early stages of deformation. With proceeding deformation, transformation decouples from carbon concentration and other factors, such as RA size, morphology and distribution,

orientation, the nature of neighboring phases, defect structure, rotation and stress state, affect the mechanical stabilization of the RA and control its stability during the later stage of the deformation.

Acknowledgements

This work was supported by the Australian Synchrotron Research Program, which was funded by the Commonwealth of Australia under the National Collaborative Research Infrastructure Strategy and by the Engineering Materials Institute, University of Wollongong (UOW). Special thanks to the XOR beamline members and the APS user office for support. Use of the APS was supported by the U.S. Department of Energy under contract DE-AC02-06CH11357. Support by the Monash Centre for Electron Microscopy is gratefully acknowledged. K. Yan appreciates Dr. M.D. Callaghan for his help of mechanical properties data analysis and contribution to the discussion section. Experimental support by Dr. Jonathan D. Almer (APS) and Mr. Thomas Schambron (formerly UOW now at BlueScope Steel Ltd.) is greatly appreciated. The authors thank A/Prof. Laichang Zhang, Edith Cowan University, formerly UOW, for providing images of heat tinted samples.

References

[1] I.B. Timokhina, P.D. Hodgson, E.V. Pereloma, Metall. Mater. Trans. A, 35A (2004) 2331-2341.

[2] V.T.T. Miihkinen, D.V. Edmonds, Mater. Sci. Technol., 3 (1987) 422-431.

[3] E.V. Pereloma, I.B. Timokhina, M.K. Miller, P.D. Hodgson, Acta Mater., 55 (2007) 2587-2598.

[4] J.B. Seol, D. Raabe, P.P. Choi, Y.R. Im, C.G. Park, Acta Mater., 60 (2012) 6183-6199.

[5] I.B. Timokhina, P.D. Hodgson, E.V. Pereloma, Metall. Mater. Trans. A, 34A (2003)

1599-1609.

[6] R. Blondé, E. Jimenez-Melero, L. Zhao, J.P. Wright, E. Brück, S. van der Zwaag, N.H. van Dijk, Acta Mater., 60 (2012) 565-577.

[7] K.-D. Liss, A. Bartels, A. Schreyer, H. Clemens, Texture Microstruct., 35 (2003) 219-252.

[8] K.-D. Liss, K. Yan, Mater. Sci. Eng., A, 528 (2010) 11-27.

[9] E. Jimenez-Melero, N.H. van Dijk, L. Zhao, J. Sietsma, J.P. Wright, S. van der Zwaag, Mater. Sci. Eng. A, 528 (2011) 6407-6416.

[10] O. Muransky, P. Sittner, J. Zrnik, E.C. Oliver, Acta Mater., 56 (2008) 3367-3379.

[11] E.C. Oliver, P.J. Withers, M.R. Daymond, S. Ueta, T. Mori, Appl. Phys. A, 74 (2002) s1143-s1145.

[12] O. Muránsky, P. Šittner, J. Zrnik, E.C. Oliver, Metall. Mater. Trans. A, 39 (2008) 3097-3104.

[13] Y. Tomota, H. Tokuda, Y. Adachi, M. Wakita, N. Minakawa, A. Moriai, Y. Morii, Acta Mater., 52 (2004) 5737-5745.

[14] N.H. van Dijk, L. Zhao, M.T. Rekveldt, H. Fredrikze, O. Tegus, E. Brück, J. Sietsma, S. van der Zwaag, Physica B: Condensed Matter, 350 (2004) E463-E466.

[15] R.J. Moat, S.Y. Zhang, J. Kelleher, A.F. Mark, T. Mori, P.J. Withers, Acta Mater., 60 (2012) 6931-6939.

[16] Z.H. Cong, N. Jia, X. Sun, Y. Ren, J. Almer, Y.D. Wang, Metall. Mater. Trans. A, 40 (2009) 1383-1387.

[17] U. Crossa Archiopoli, N. Mingolo, N. Mingolo, Surf. Coat. Technol., 202 (2008) 5982-5990.

[18] P.J. Jacques, Q. Furnemont, S. Godet, T. Pardoen, K.T. Conlon, F. Delannay, Philos Mag, 86 (2006) 2371-2392.

[19] N. Jia, Z.H. Cong, X. Sun, S. Cheng, Z.H. Nie, Y. Ren, P.K. Liaw, Y.D. Wang, Acta Mater., 57 (2009) 3965-3977.

[20] K. Asoo, Y. Tomota, S. Harjo, Y. Okitsu, ISIJ Int., 51 (2011) 145-150.

[21] W. Woo, V.T. Em, E.Y. Kim, S.H. Han, Y.S. Han, S.H. Choi, Acta Mater., 60 (2012) 6972-6981.

[22] D.L. Bourell, A. Rizk, Acta Metall., 31 (1983) 609-617.

[23] K. Yan, D.G. Carr, S. Kabra, M. Reid, A. Studer, R.P. Harrison, R. Dippenaar, K.-D. Liss, Adv. Eng. Mater., 13 (2011) 882-886.

[24] R.K. Dutta, R.M. Huizenga, M. Amirthalingam, A. King, H. Gao, M.J.M. Hermans, I.M. Richardson, Scripta Mater., 69 (2013) 187-190.

[25] P. Jacques, Q. Furnemont, A. Mertens, F. Delannay, Philos. Mag. A, 81 (2001) 1789-1812.

[26] B. Clausen, Risø National Laboratory, Roskilde, Denmark, 1997.

[27] A.A. Saleh, E.V. Pereloma, A.A. Gazder, Acta Mater., 61 (2013) 2671-2691.

[28] M.R. Daymond and H.G. Priesmeyer, Acta Mater., 50 (2002) 1613-1626.

[29] E.C. Oliver, M.R. Daymond, P.J. Withers, Acta Mater., 52 (2004) 1937-1951.

[30] R. Dakhlaoui, A. Baczmański, C. Braham, S. Wroński, K. Wierzbanowski, E.C. Oliver, Acta Mater., 54 (2006) 5027-5039.

[31] S.A. Kim, W.L. Johnson, Mater. Sci. Eng. A, 452-453 (2007) 633-639.

[32] G.K. Tirumalasetty, M.A. van Huis, C. Kwakernaak, J. Sietsma, W.G. Sloof, H.W. Zandbergen, Acta Mater., 60 (2012) 1311-1321.

[33] Q. Furnemont, M. Kempf, P.J. Jacques, M. Goken, F. Delannay, Mater. Sci. Eng., A, A328 (2002) 26-32.

[34] K. Davut, S. Zaefferer, Steel Research International, 83 (2012) 584-589.

[35] X.C. Xiong, B. Chen, M.X. Huang, J.F. Wang, L. Wang, Scripta Mater., 68 (2013) 321-

324.

[36] M.X. Zhang, P.M. Kelly, Mater. Charact., 40 (1998) 159-168.

[37] N. van Dijk, A. Butt, L. Zhao, J. Sietsma, S. Offerman, J. Wright, S. van der Zwaag, Acta Mater., 53 (2005) 5439-5447.

[38] K.-D. Liss, D. Qu, K. Yan, M. Reid, Adv. Eng. Mater., 15 (2013) 347-351.

[39] J.S. Fisher, Holloman, J.H., Turnbull, D., T Am I Min Met Eng, 185 (1949) 691-700.

[40] E.R. Morgan, T. Ko, Acta Metall., 1 (1953) 36-48.

[41] A. Itami, M. Takahashi, K. Ushioda, ISIJ Int., 35 (1995) 1121-1127.

[42] S.O. Kruijver, L. Zhao, J. Sietsma, S.E. Offerman, N.H. van Dijk, E.M. Lauridsen, L. Margulies, S. Grigull, H.F. Poulsen and S. van der Zwaag, J. Phys. IV, 104 (2003) 499-502.

[43] G.K. Tirumalasetty, M.A. van Huis, C. Kwakernaak, J. Sietsma, W.G. Sloof, H.W. Zandbergen, Scripta Mater., 71 (2014) 29-32.

[44] I.B. Timokhina, P.D. Hodgson, E.V. Pereloma, Metall. Mater. Trans. A, 38 (2007) 2442-2454.

[45] E. Pereloma, A. Gazder, I. Timokhina, The Transformation-Induced Plasticity Effect and the Stability of Retained Austenite in Steels, in: R. Colas and G.E. Totten (Eds.) Encyclopedia of Iron, Steel and their Alloys, Taylor and Francis, 2015.

Figure(s)

Figure 1a

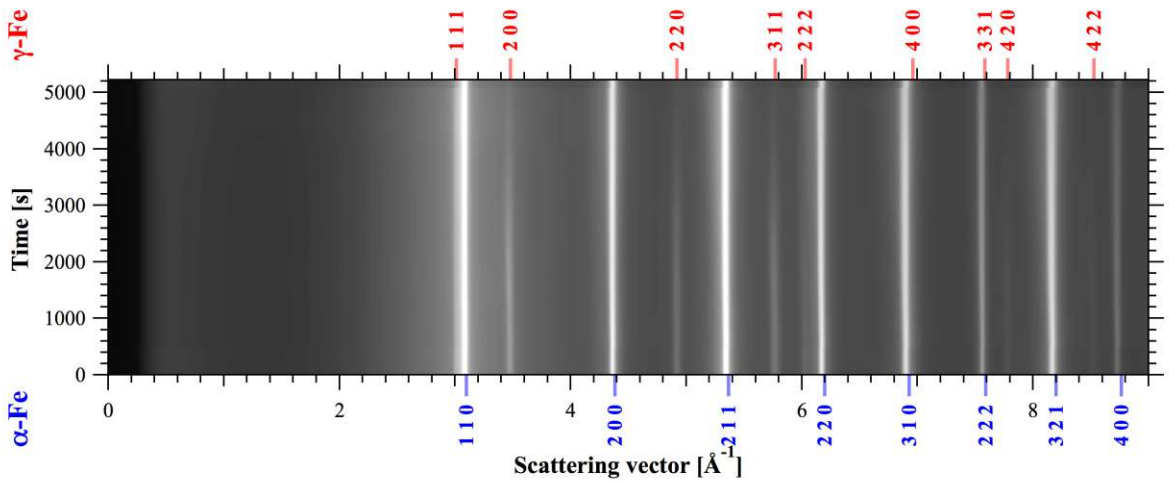

Figure 1b

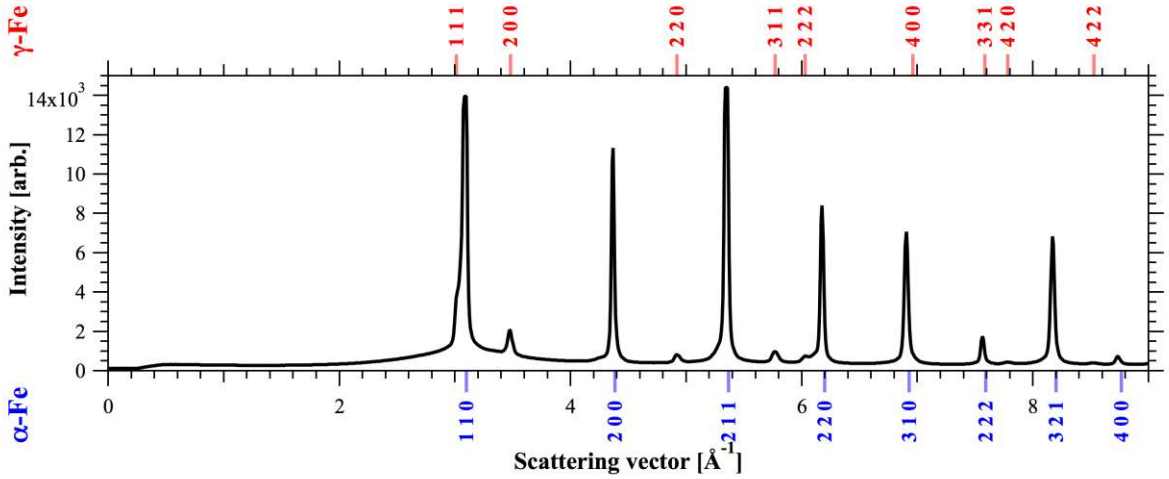

Figure 1c

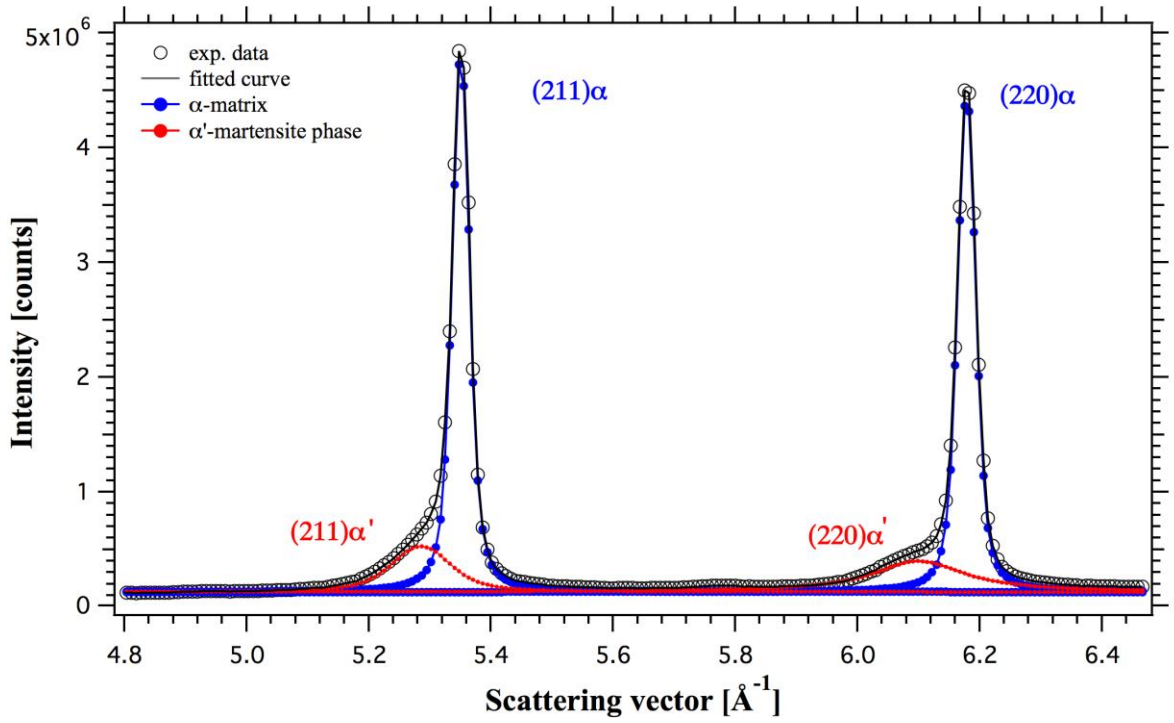

Fig. 1. In situ diffraction observation of sample TMP-770, where (a) diffraction intensity is plotted in gray scale as a function of time during tensile testing; (Light-high intensity, dark-low intensity); (b) diffraction intensity of the as-received material from sample TMP-770 is plotted against the scattering vector. Reflections from α-matrix (α-Fe) and austenite phase (γ-Fe) are indexed; and (c) Deconvolution of martensite phase from α-matrix.

Figure 2

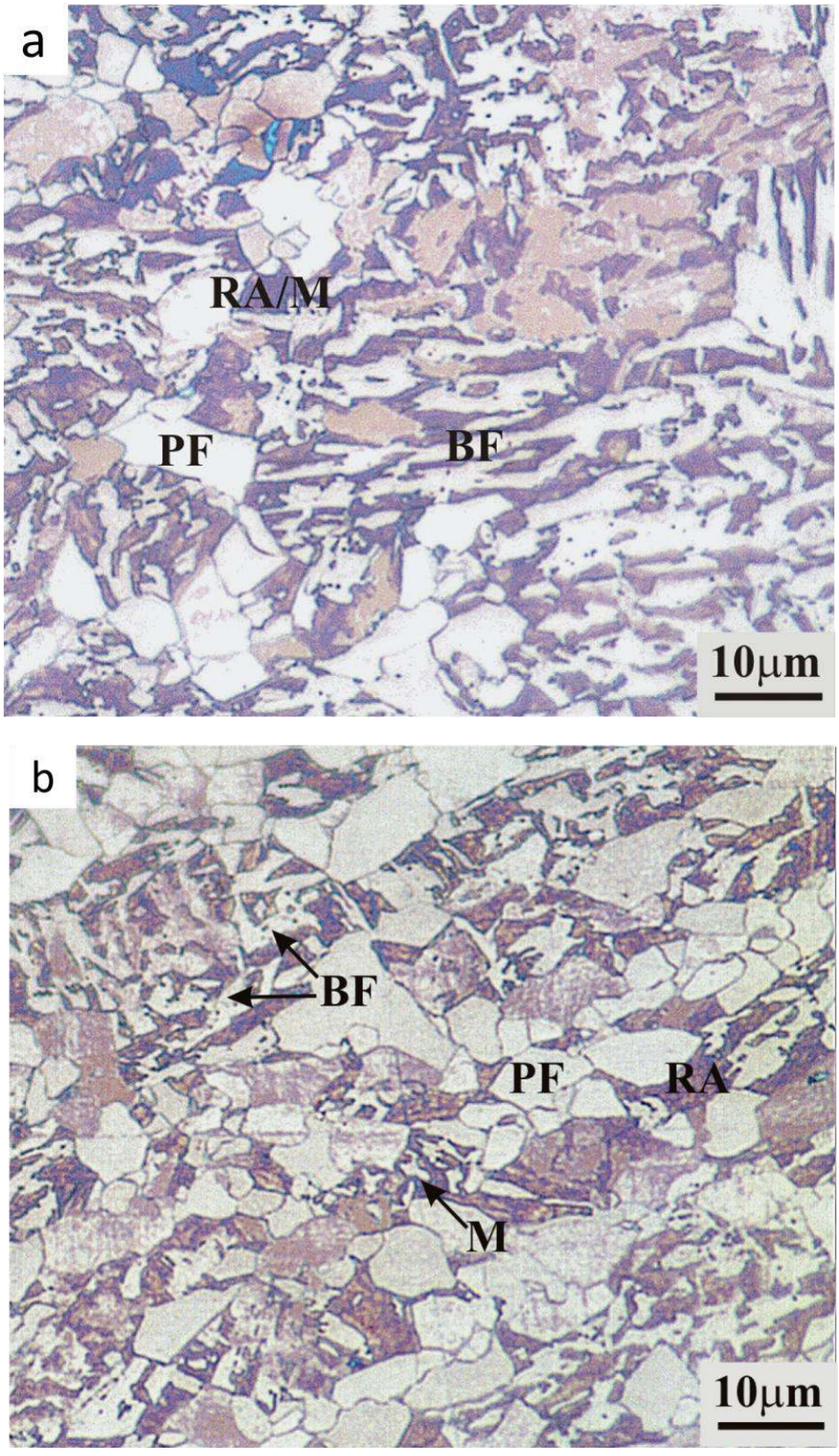

Fig. 2. Optical micrographs of the thermo-mechanical processed of the samples TMP-790 (a) and TMP-770 (b). BF: Bainitic Ferrite (white/light brown); PF: Polygonal Ferrite (light); RA: Retained Austenite (dark maroon); M: Martensite (blue).

Figure 3

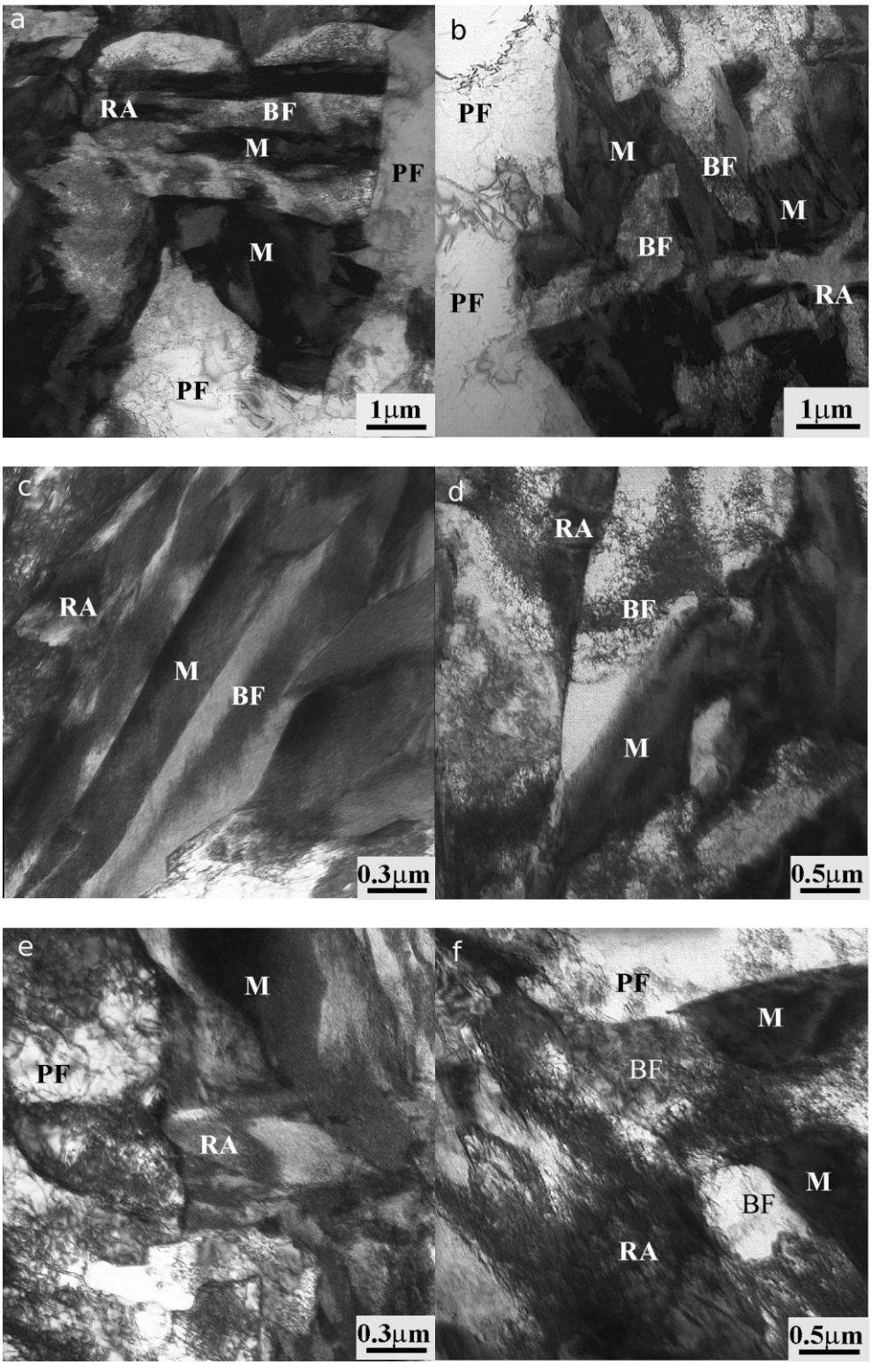
a
RA
BF
M
PF
M
PF
1μm
b
PF
M
BF
M
BF
PF
RA
1μm
c
RA
M
BF
0.3μm
d
RA
BF
M
0.5μm
e
M
PF
RA
0.3μm
f
PF
M
BF
M
BF
RA
0.5μm

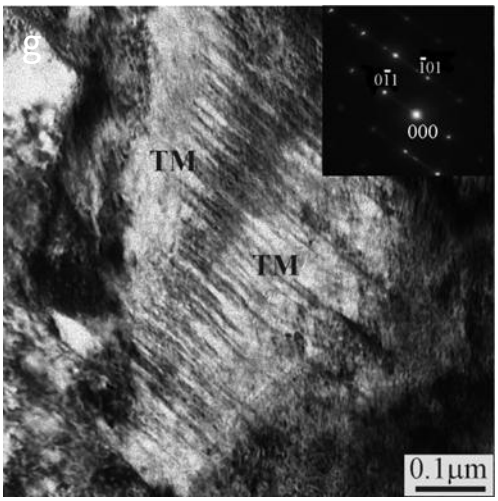

Fig. 3. Representative TEM micrographs of the steel for samples TMP-790 (a, c, e) and TMP-770 (b, d, f, g) interrupted ferrite formation temperatures. (BF-bainitic ferrite, RA-retained austenite, M-martensite, PF: polygonal ferrite, TM: twinned martensite). Inset in g: zone axis is [111] and (211) is the twinning plane.

Figure 4a

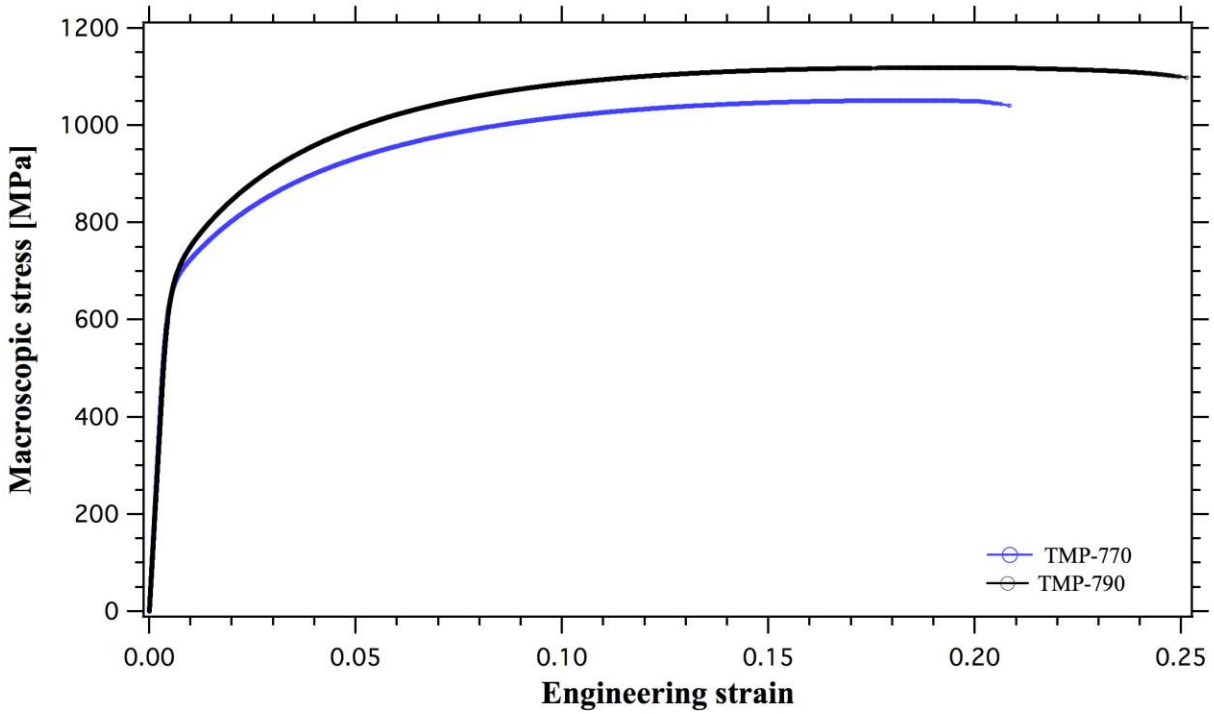

Figure 4b

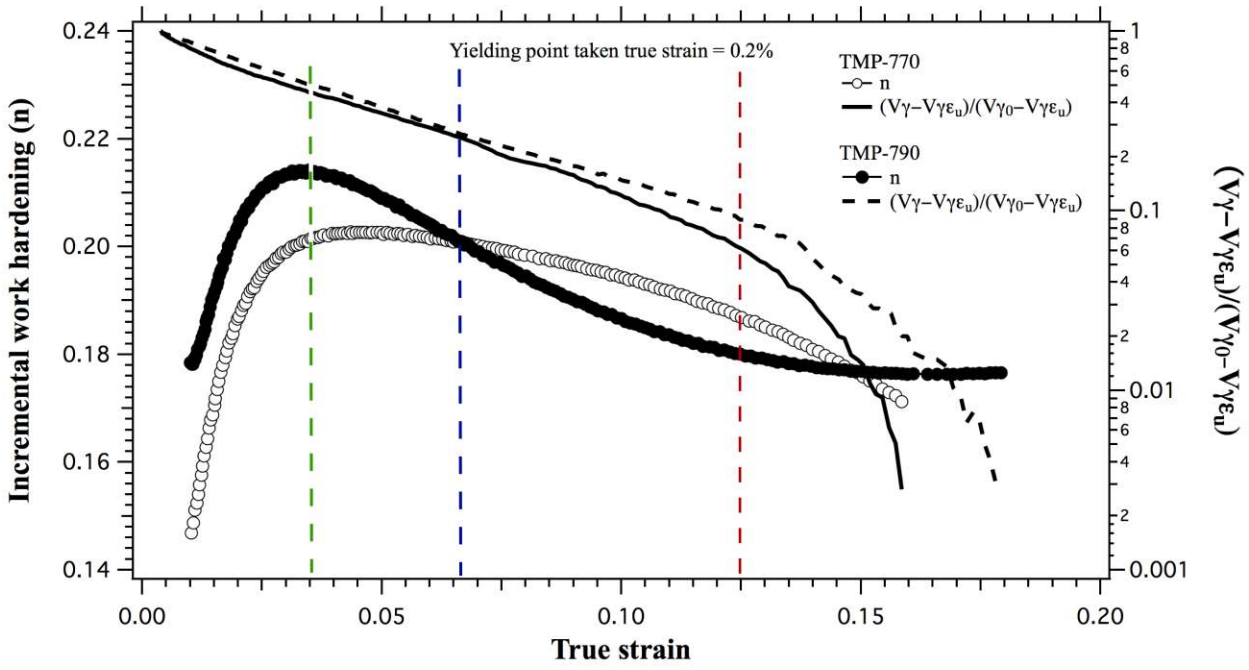

Figure 4c

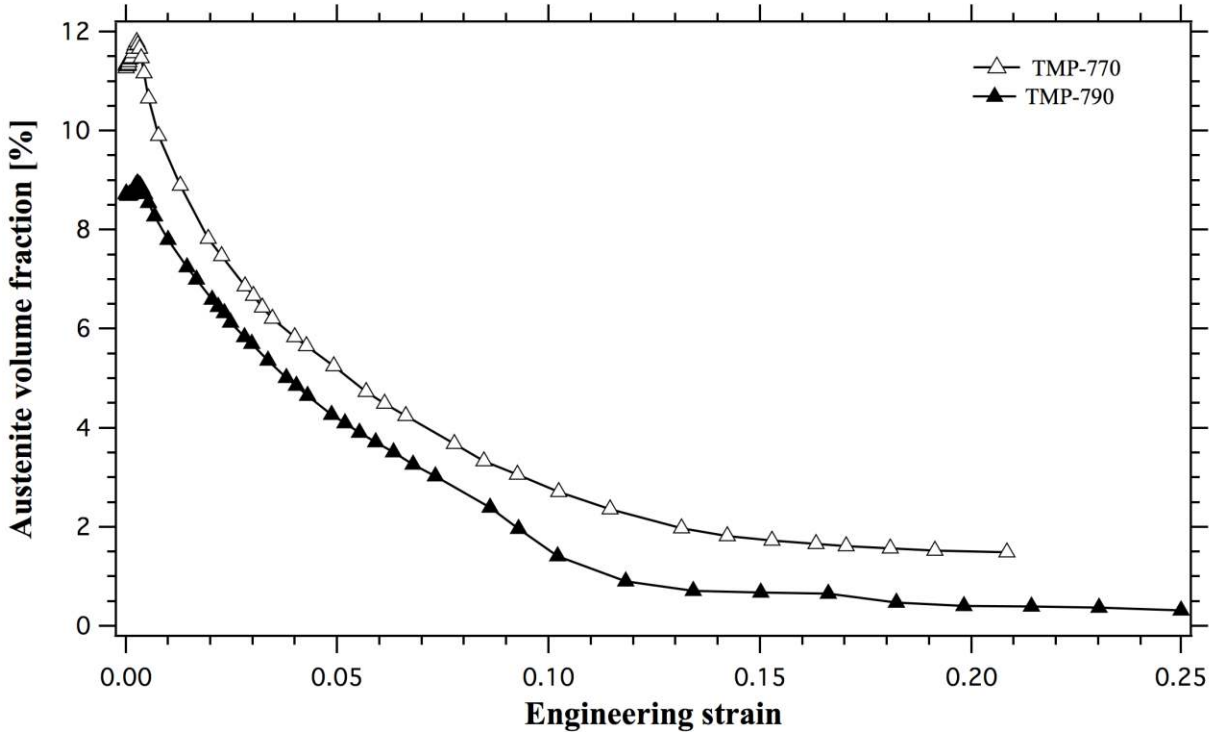

Fig. 4. (a) The engineering strain-stress responses of sample TMP-770 (blue, lower curve) and TMP-790 (black, upper curve); (b) incremental work-hardening curves (n) of TMP-770 (hollow round symbol) and TMP-790 (solid round symbol), variations of the transformable austenite as a function of true strain for the different specimens of TMP-770 (black solid line) and TMP-790 (black dashed line); and (c) the volume fraction of RA changes with macroscopic strain for specimen TMP-770 (hollowed triangle) and TMP-790 (solid triangle). Phase fraction uncertainty is estimated to be +/-5% of the displayed value. In 4b, the green dashed line at strain of 0.035 indicates the maximum point of incremental work hardening n for the two specimens; before the strain reaches 0.067, where the blue line shows, the austenite to martensite phase transformation speed is very close for sample TMP-770 and TMP790; from the strain of 0.125 onwards, the transformation of retained austenite phase in sample TMP-770 is seen to occur much faster than in sample TMP-790.

Figure 5a

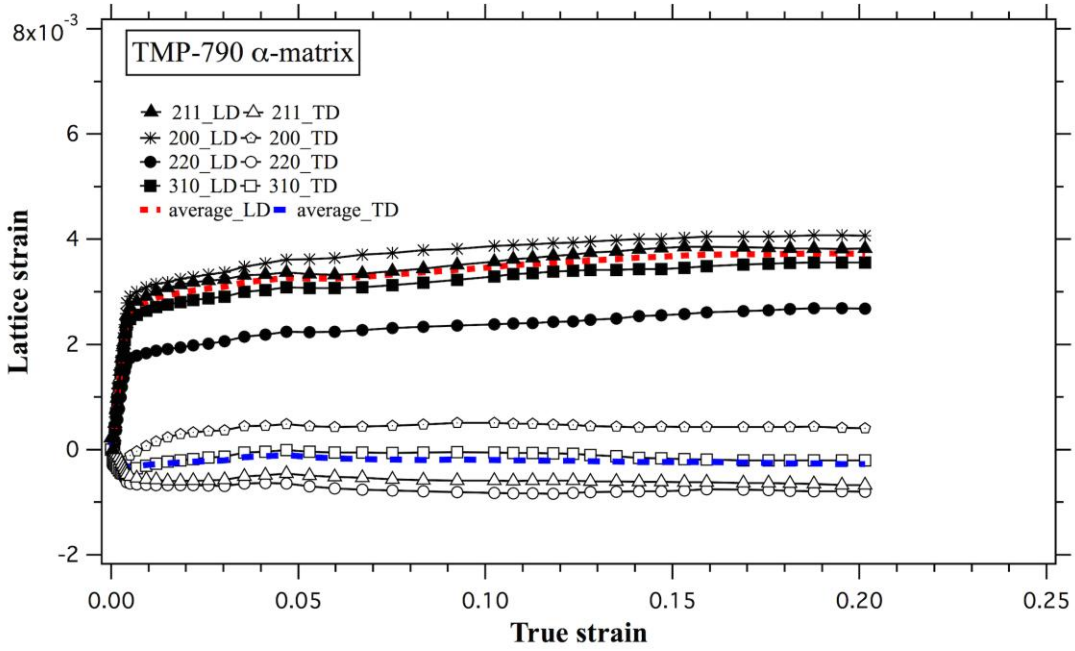

Figure 5b

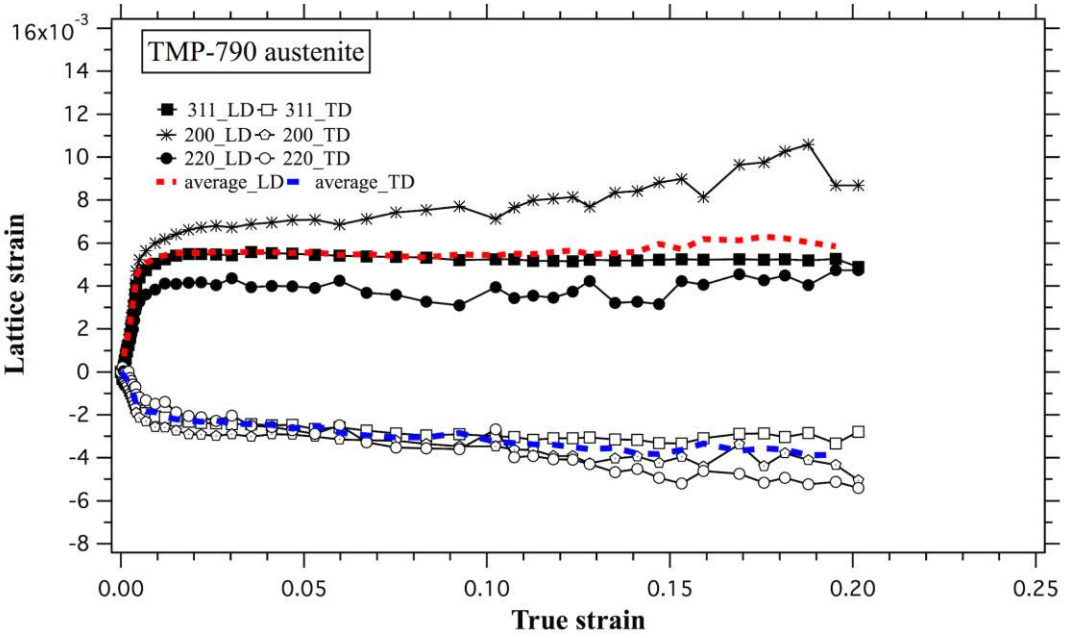

Fig. 5. Evolution of lattice strain along LD and TD for different reflections and their weight averaged value of (a) α-matrix and (b) austenite phase in sample TMP-790.

Figure 6a

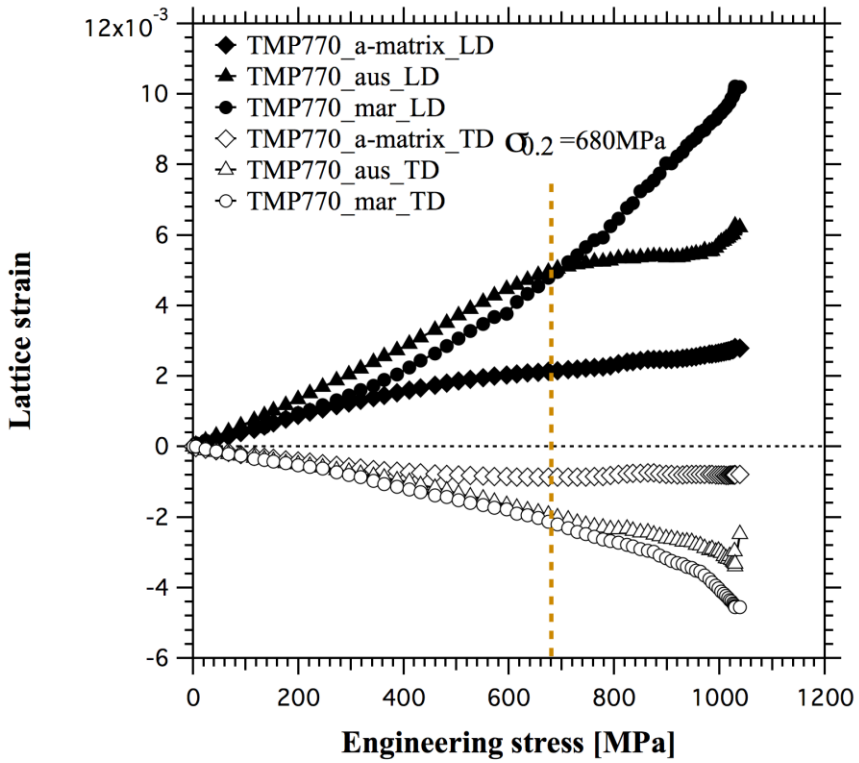

Figure 6b

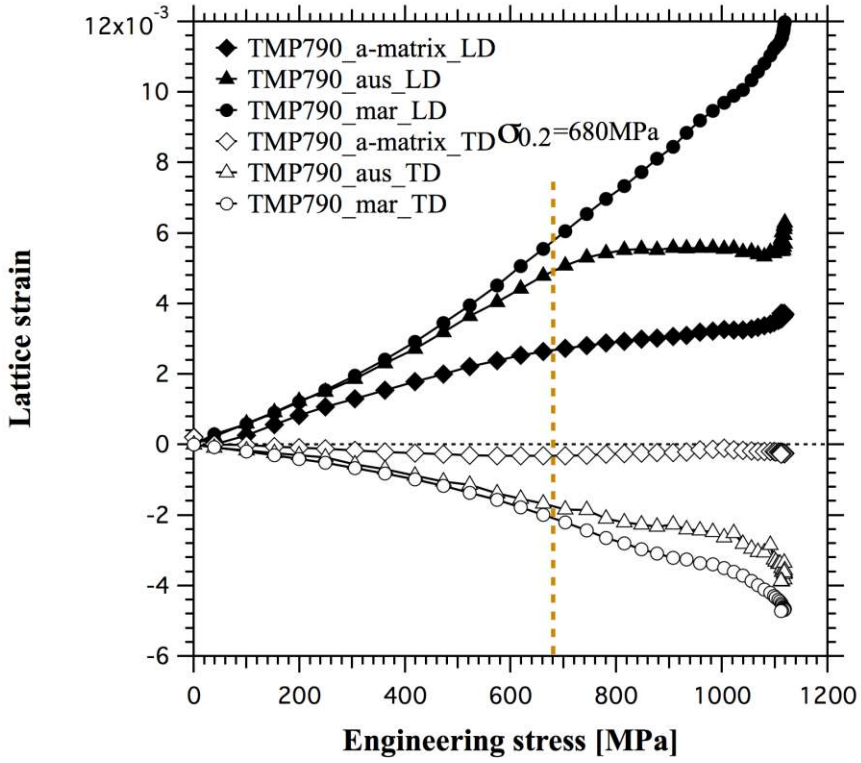

Fig. 6. Phase lattice strain of α–matrix, austenite and martensite in sample (a) TMP-770 and (b) TMP-790 as a function of macroscopic stress.

Figure 7a

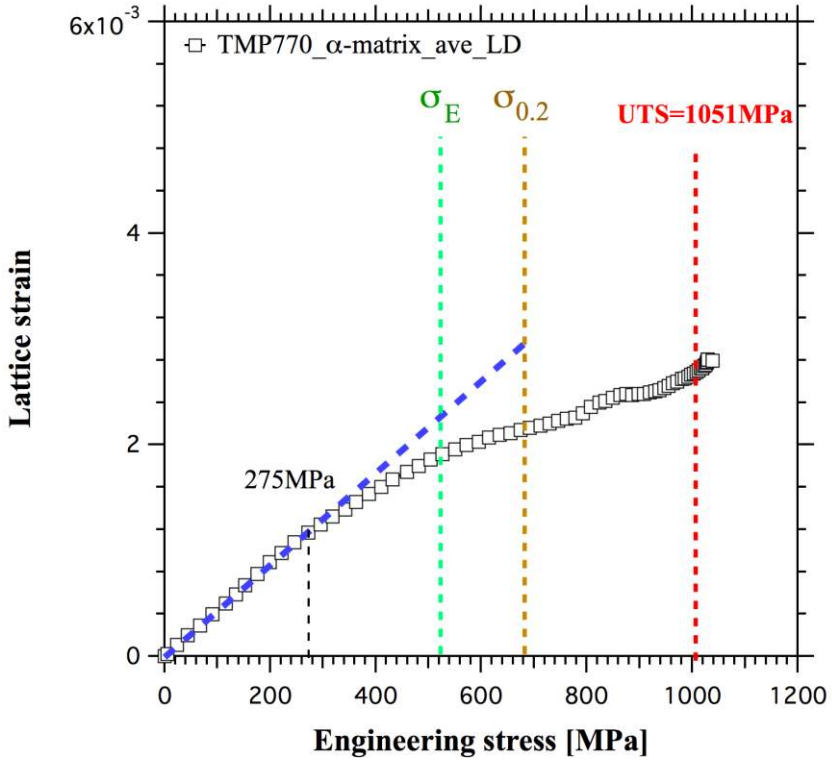

Figure 7b

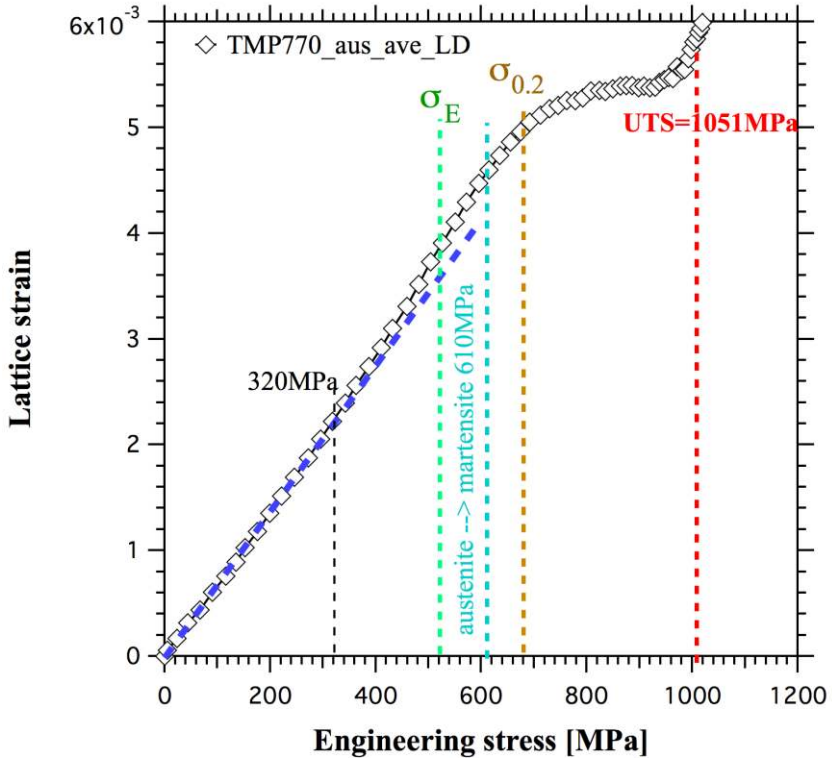

Figure 7c

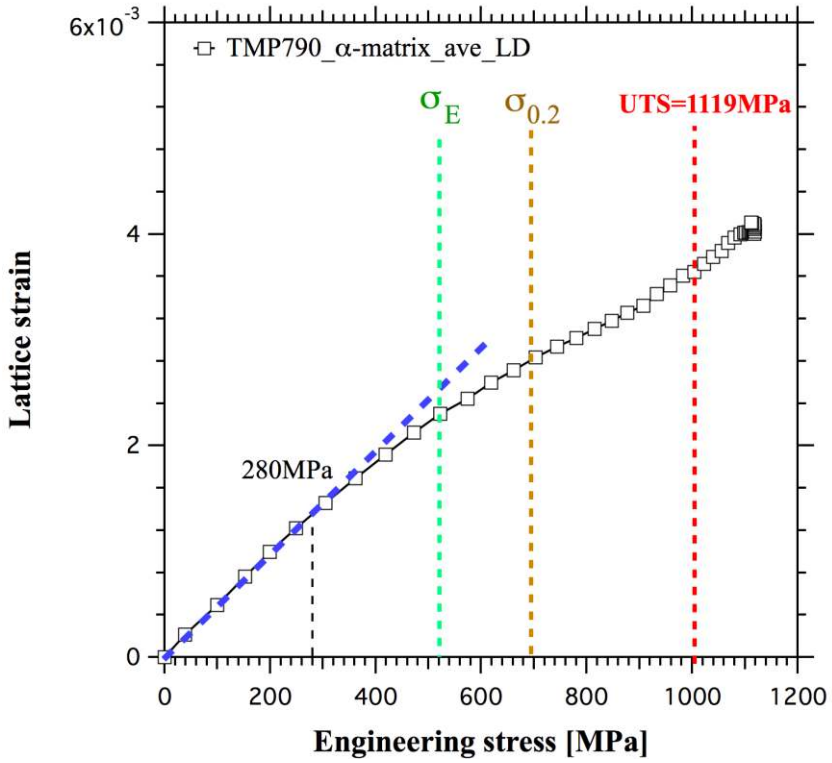

Figure 7d

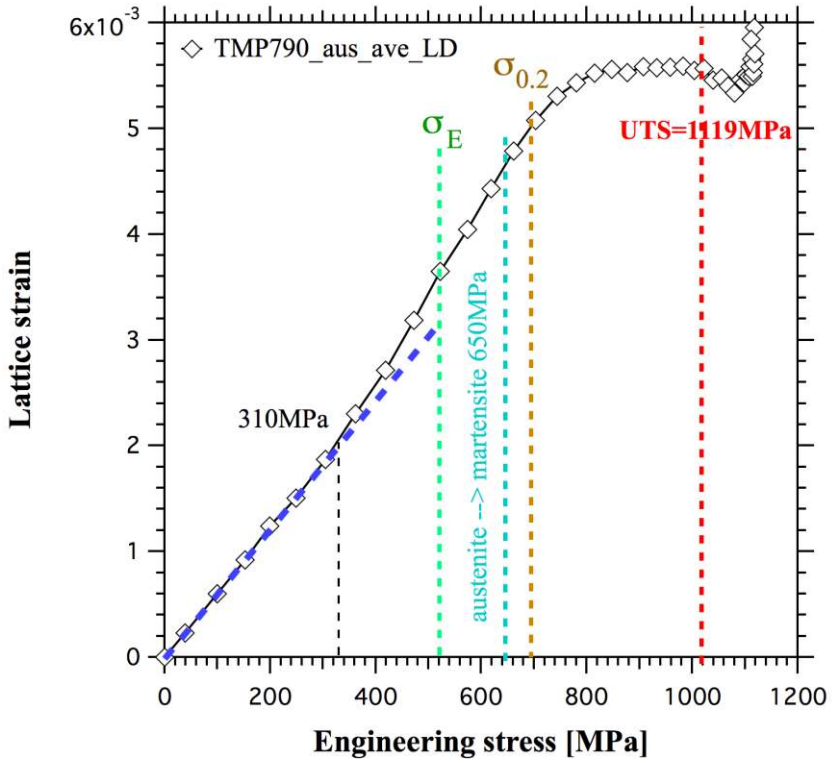

Fig. 7. The phase lattice strain of (a,c) α-matrix, (b,d) austenite phase for samples (a,b) TMP-770

and (c,d) TMP-790 changes with engineering strain during tensile test. The first dashed line (black) indicates the lattice strain starting to deviate from linear change; the green dashed line σ_E indicates the end of elastic region for the multi-phase structure; the yellow dashed line $\sigma_{0.2}$ represents the proof stress and the ultimate tensile stress is marked as red dashed; additionally, the blue dashed line marks the austenite to martensite phase transformation point in graphs b and d.

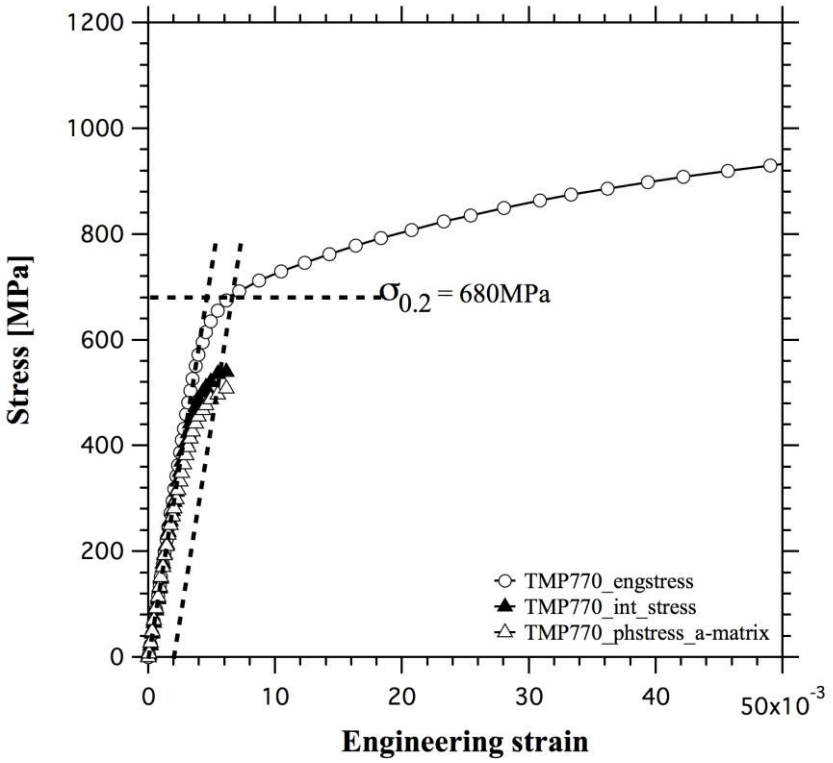

Figure 8a

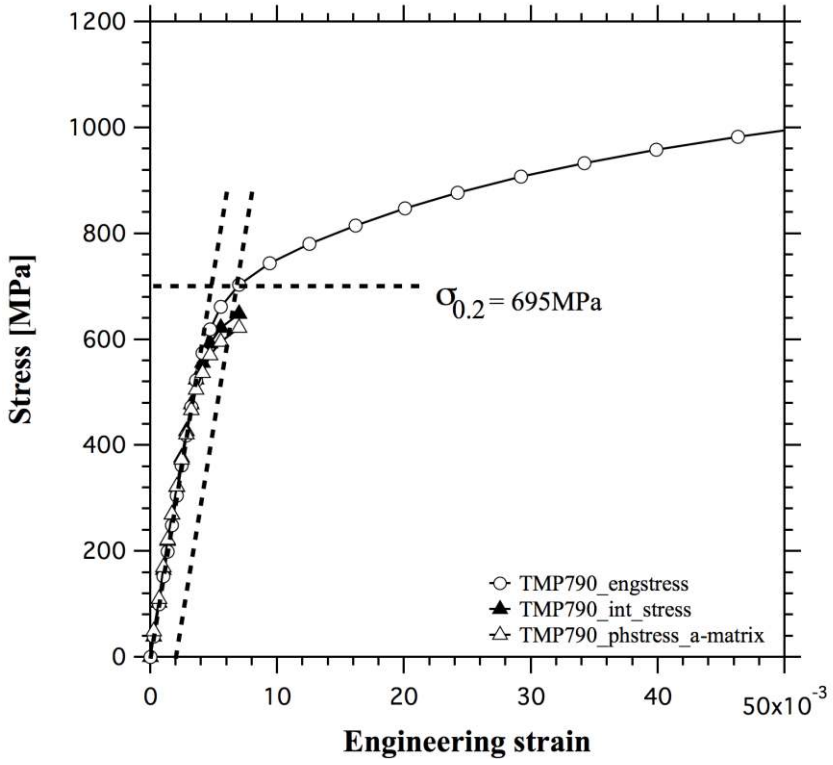

Figure 8b

Fig. 8. The α-matrix phase stress, integrated phase stress of austenite and α-matrix, as well as the macroscopic stress, plotted against engineering strain for sample (a) TMP-770 and (b) TMP-790. The black dashed lines indicate the proof stress $\sigma_{0.2}$.

Figure 9

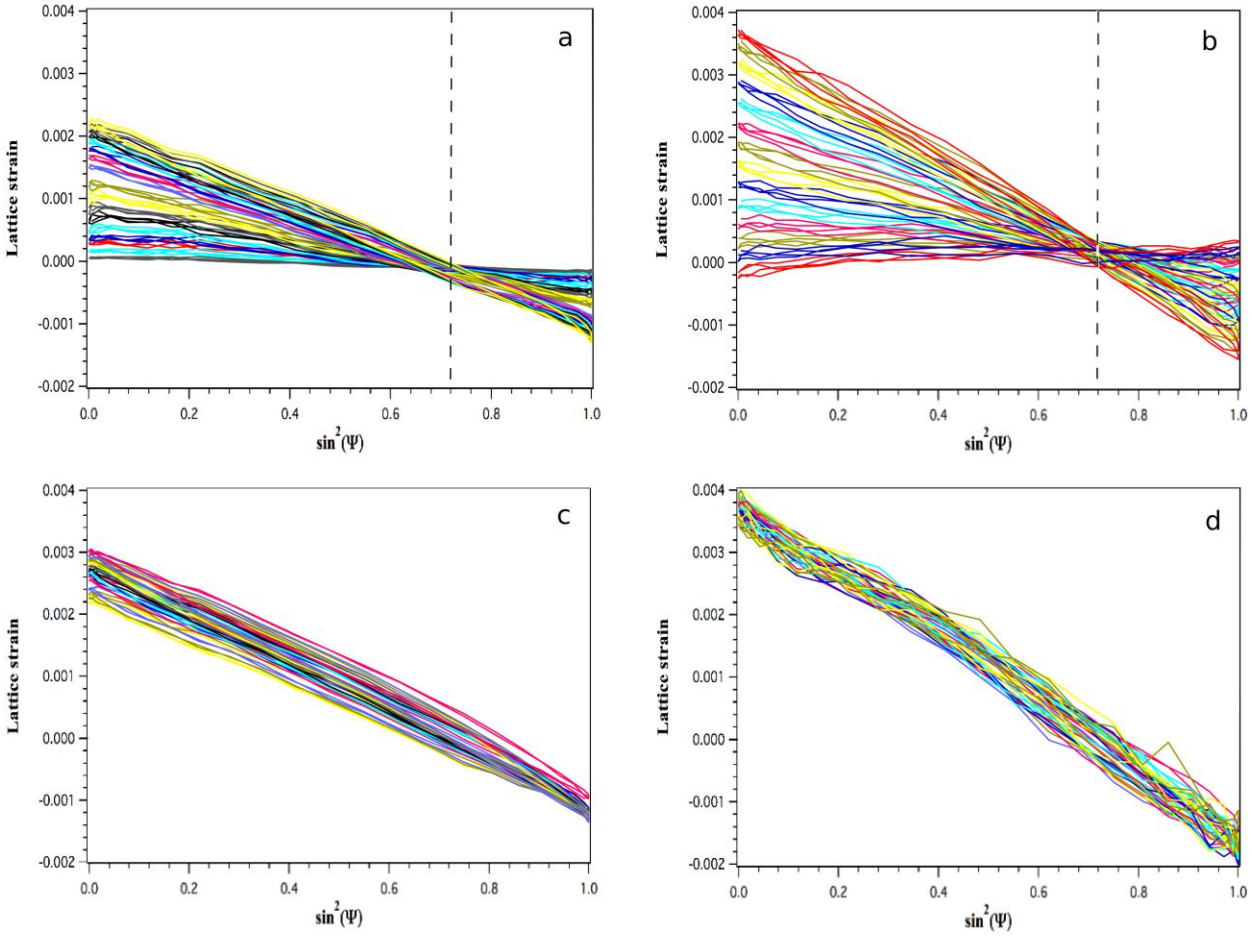

Fig. 9. Lattice strain vs. $\sin^2(\Psi)$ distributions for (a, c) reflection 211 of α-matrix and (b, d) reflection 311 in austenite phase. Graphs (a) and (b) indicate the lattice strain in the elastic region, while (c) and (d) represents the lattice strain in the plastic region. Each line represents a single diffraction Debye-Scherrer ring from reflection α-211 and γ-311, respectively, at certain macroscopic deformation levels. For clarity, only one result out of every 20 diffraction images is shown.

Figure 10

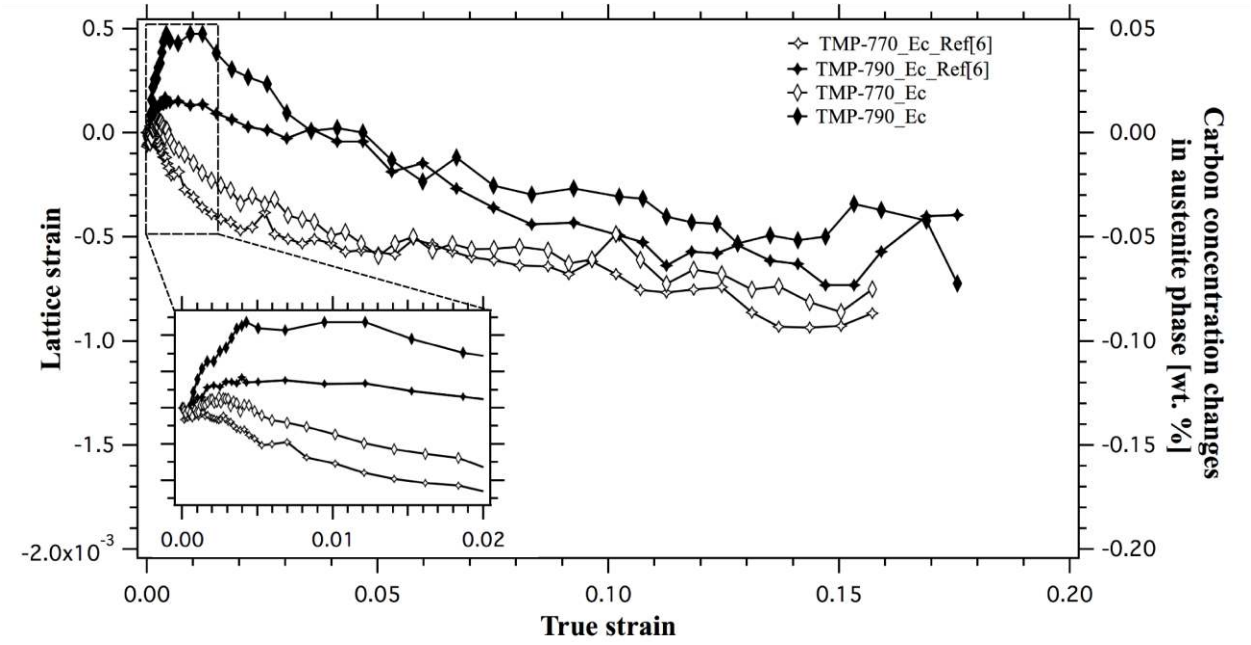

Fig. 10. The change of lattice strain (ε_c) in austenite phase that is attributed to the variation of carbon concentration, plotted against true strain. Details for true strain from 0 to 0.02 are inserted at the left bottom corner.

Table(s)

Table 1. Chemical composition of the Fe-Nb-Mo-Al TRIP steel in mass percentage.

C	Si	Mn	Al	Mo	Nb	Fe
0.21	1.18	1.52	0.57	0.29	0.036	Balance

Table 2. Macroscopic parameters characterized during synchrotron experiment for the mechanical response of sample TMP-770 and TMP-790 to the applied tensile stress.

Specimen	Yield stress (MPa)	Ultimate tensile stress (MPa)	Elongation at fracture (%)
TMP-770	680	1051	21
TMP-790	695	1119	25